Density Troughs in the Ionosphere Sustained by Transport Barriers

M.A. Malkov[1,*] , V.I. Sotnikov[2], and E.V. Mishin[3,†]

[1]University of California, San Diego, La Jolla, CA 92093, USA
[2]Naval Research Laboratory, Washington DC, 20375
[3]Retired from the Air Force Research Laboratory

Key Points:

- Density troughs formed in the Earth's ionosphere are likely to develop fast gradient instabilities but typically live longer than expected
- We argue that while driving turbulent plasma transport along the density gradient, the drift-wave instability also generates macroscopic (zonal) flows across the gradient and magnetic field
- Zonal flows efficiently self-regulate the instability-transport relation, essentially suppressing the two

*orcid:0000-0001-6360-1987
†orcid:0000-0002-3183-0600

Corresponding author: M. A. Malkov, `mmalkov@ucsd.edu`

Abstract

This study explores the relaxation and sustainability of density irregularities and plasma flows in the Earth's ionosphere. To do this, we use a modified model of drift-wave turbulence known as the Hasegawa-Wakatani model. Similar to turbulent processes in laboratory plasmas, we explore a powerful mechanism that can reduce the turbulent plasma transport. This mechanism is associated with the creation of 'zonal flows,' cutting across the gradients of particle density and magnetic fields. They work effectively to minimize particles' random movement and reduce the turbulence causing this movement. The zonal flows create transport barriers in areas where the density gradient is steepest and where drift waves grow most vigorously. The transport barriers significantly delay the refill of low-density regions with surrounding plasma. They also lead to changes in the electric potential of the plasma and influence the movement of ions in the direction of the magnetic field. Our research investigates how these zonal flows are generated and how effectively they sustain density irregularities. We also examine the spectral characteristics of turbulence in and around these barriers.

1 Introduction

During active geomagnetic conditions, midlatitude and subauroral ionosphere just equatorward of the auroral zone often becomes disturbed by a number of phenomena that could adversely affect modern technology. In particular, the disturbed subauroral convection is dominated by enhanced, westward, $\mathbf{V} = \mathbf{V}_W$, plasma streams: narrow subauroral ion drifts (SAID) near midnight and broad subauroral polarization streams (SAPS) on the duskside, containing deep-density depletions, manifested in troughs elongated in the magnetic field direction (e.g., Foster & Burke, 2002; E. V. Mishin, 2013). Plasma density irregularities inside subauroral irregular plasma density troughs (e.g., Mishin et al., 2003; Sinevich et al., 2022) may induce scintillations in radio waves transmitted by GNSS or communication satellites, thus affecting the quality of received signals (e.g., Basu et al., 2001; Ledvina et al., 2002; Nishimura et al., 2021; Pradipta et al., 2023). While the SAID and SAPS onsets are close to that of magnetospheric substorms, e.g., (E. Mishin et al., 2017), the phenomena typically last a few more hours well into the substorm recovery (e.g., He et al., 2017). Various scenarios for the SAID and SAPS generation have been critically ascertained by E. V. Mishin (2023).

The discovery (MacDonald et al., 2018) of peculiar subauroral arcs – Strong Thermal Emission Velocity Enhancement (STEVE) and the picket fence – inside extremely high speed and electron temperature SAID channels with deep troughs instigated a series of systematic observational efforts, both spacecraft- and ground-based (see a comprehensive review by (Nishimura et al., 2023), complemented with theoretical modeling (e.g., Liang et al., 2021, 2022; E. V. Mishin & Streltsov, 2024). The observations testify to intrinsic mechanisms of sustainability, self-organization, and ultimate disruption of SAID. Indeed, the density and temperature gradients such as at the SAID density walls and strong $\mathbf{E}\times\mathbf{B}$ shear flows have long been recognized as potentially efficient drivers of several instabilities (Tsunoda, 1988). Should they develop without a significant back-reaction from the SAID to sustain its structure, the unstable waves would likely grow to the point of SAID disruption.

An example of ionospheric structures pertinent to the present study and in which steep density gradients form is equatorial spread F (ESF) plasma bubbles. They were studied theoretically in (e.g., Ossakow & Chaturvedi, 1978; Ott, 1978). The ESF bubbles are frequently accompanied by very fast ion drifts (Huang et al., 2007), as shown in one observation example in Fig.1 from (Huang et al., 2007). In this particular case, the DMSP spacecraft crosses the ESF plasma bubble just south of the magnetic equator, detecting the plasma density drops by more than two orders of magnitude. The vertical velocity has two peaks inside the bubble at 2000 m/s. The westward velocity has

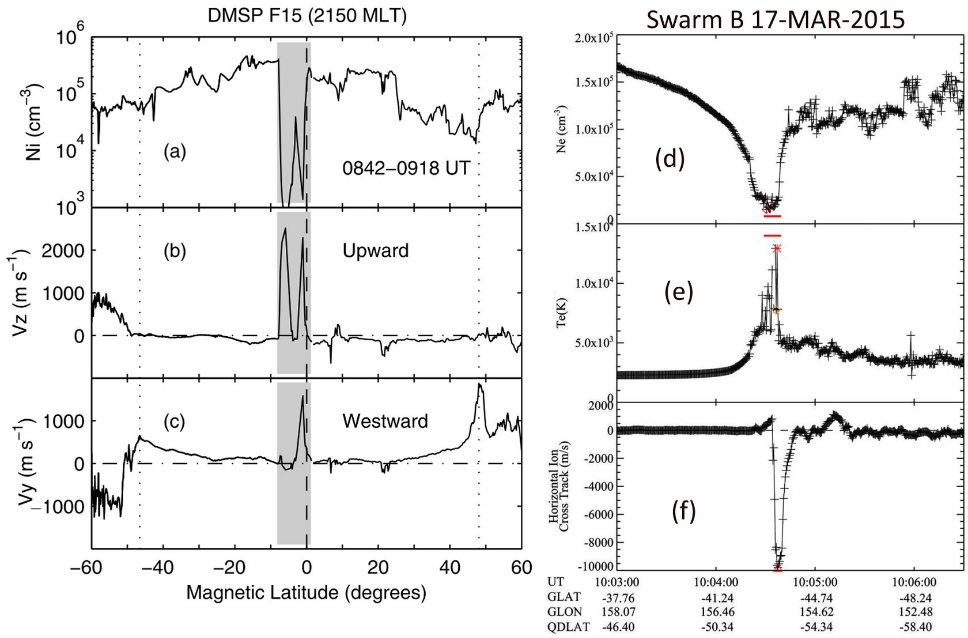

Figure 1. (left column) Adopted from (Huang et al., 2007) with authors' permission including the following caption: Latitudinal distribution of the ionospheric ion density and velocity measured by the (a) DMSP F15 satellite between 0842 and 0918 UT on 29 October 2003. V_z is the vertical velocity component, and V_y is the horizontal velocity component. The shaded regions indicate deep density depletion. The vertical dotted lines indicate the location of the ion horizontal velocity peak in the SAPS region. (right) Adopted from (Martinis et al., 2022) with authors' permission: Plasma parameters measured along the Swarm B trajectory in the Northern Hemisphere mapped to 425 km in the Southern Hemisphere. From top to bottom: electron density (N_e), electron temperature (T_e), and horizontal plasma drift velocity (V_hor).

only one strong peak inside the bubble that reaches 1500 m/s. This flow morphology indicates that the two jets inside the bubble are not collinear. *For generality, we also show the SAID channel detected by the Swarm-B satellite at about 500 km altitude during a bright STEVE arc event (Martinis et al., 2022). Such* $\delta T_\mathrm{e} - \delta n_\mathrm{e} - \delta V_\mathrm{hor}$ *variation across the channel is typical for strong SAID events. Frequently, the upward vertical flow velocity is also enhanced inside SAID channels.*

One may distinguish between two scenarios of a turbulent relaxation of a steep density gradient after the driver that creates this gradient is switched off. For the sake of argument, let us consider an isolated plasma layer with strong density gradients across the magnetic field between two broader plasma regions with constant densities. The first scenario can be termed quasi-linear. It could occur when the underlying instability wears out its source. For example, the density profile or velocity shear can be flattened by a turbulent density and momentum transport, respectively. Unstable small-scale flow irregularities, comparable with the ion-acoustic gyroradius, drive the transport. Under the second scenario, instability takes a more violent route by forming large coherent structures, which cut across the flow. This avenue of plasma transport is often associated with strong eddies, blobs, streamers, or even avalanches (e.g., Carreras et al., 1998; Zweben et al., 2003; Garcia et al., 2005; Dippolito et al., 2011). The avalanches promptly transport material and heat across the main flow. These transport regimes relax the density and temperature gradients much faster than in the quasi-linear scenario. For example, the coherent flow disruption can occur in a matter of turnover time of large eddies. This second possibility is often characterized as an avalanche transport regime. The first, relatively benign, transport mechanism is often quantified by the Bohm diffusivity, $D_B = cT_i/16eB$. Moreover, it can be further reduced to the so-called gyro-Bohm regime, $D_{gB} \sim D_B \rho_s / L_n$. Here $\rho_s = \sqrt{T_e/M}\omega_{ci}^{-1}$ is the ion-acoustic gyro-radius, ω_{ci} is the ion gyro-frequency, and L_n^{-1} is the characteristic density gradient.

However, flattening the *SAID may take more than a few hours*(e.g., He et al., 2017). If the Kelvin-Helmholtz instability were advancing in the SAID shear flow, large eddies would mix the density and temperature much earlier. In addressing this dilemma, it is helpful to turn to its analogy with magnetic plasma confinement in laboratory devices, such as tokamaks and stellarators, discussed in the above references. We have learned that there is a third scenario in which the transport-driving turbulence exhibits an inverse cascade of unstable drift wave (DW) perturbations across the magnetic field that self-organize in alternating streams comprising a shear flow. These streams, termed zonal flows (ZF), are directed across the magnetic field and the instability-driving density/temperature gradients. The flows react back to the wave instability and associated particle transport in two ways. First, they stretch DW eddies by imposing a shearing motion on them. This shortens the scale of the eddies across the ZF, thus leading to turbulence damping. However, the damping does not erase the DWs completely, as they maintain the ZF itself. Even if a nearly complete turbulence suppression happens temporarily, the instability resumes, and the process may evolve in a limit-cycle oscillation regime (e.g., Malkov et al., 2001; E.-J. Kim & Diamond, 2003; Diamond et al., 2005; Malkov & Diamond, 2009; Estrada et al., 2011; Schmitz et al., 2012; Dam et al., 2013).

Second, ZFs affect the plasma transport itself. It comes from the suppression, as mentioned earlier, of the transport-driving DW eddies and their stretching across the density gradient. It follows that an efficient suppression of turbulent transport and preservation of a plasma trough may be achieved by nonlinear feedback from the instability to maintain the ZF. Mechanisms of self-organization and self-sustainability are well-known in magnetic fusion and geophysical fluid dynamics research areas. Magnetically isolated plasma structures supported by strong ExB shear flows have been studied for decades. Their generation and control became an instrument of choice for the particle and heat flux suppression in the magnetic fusion devices after the discovery of the so-called H-mode plasma confinement in the ASDEX Tokamak (Wagner et al., 1982). Here, 'H' stands for the "high" confinement regime that emerges from the L-mode (low) confinement regime characterized by an enhanced turbulent transport across the field (see Diamond et al., 2005; Hahm & Diamond, 2018; Groebner & Saarelma, 2023, for review). The transport driving DW turbulence is generated by confined plasma's temperature and density gradients, thus severely restricting the confinement quality and duration. The transition to the H-mode occurs when Reynolds stresses, built up by the DW eddies, generate the above-discussed ZFs.

Significant differences exist between the transition mechanisms to the H-mode in magnetic fusion devices, resulting in steep density, temperature gradients, and ionospheric troughs. However, building up Reynolds stresses in turbulence is generic. Its role in maintaining shear flows along the walls of the troughs needs to be investigated once gradient-driven instabilities are present in such systems. This mechanism enhances the trough lifetime and controls the spectrum of turbulence. It emerges from a delicate balance between the turbulence energy input at short scales from the instability, an inverse cascade accelerating the flow, and a forward cascade where the unused fluctuation energy dissipates. These processes are coordinated in such a way as to leave the turbulence level at a bare minimum, thus also minimizing the transport. Unsurprisingly, ZFs are not robust, but they are not exceptional either. Once established, they typically remain stable and self-sustaining within certain boundaries in the parameter space. Upon crossing these boundaries, a strong Kelvin-Helmholtz instability may set in, resulting in large eddies that disrupt the flow. Overall, this process would constitute a tertiary instability of the initial plasma configuration (Rogers et al., 2000; Numata et al., 2007). The first two are the DW instability driven by the density and pressure gradients, followed by the secondary instability constituting the amplification of the ZF.

The objectives of the present study are (i) to extend our understanding of the mechanisms whereby significant density and temperature contrasts are maintained in the subauroral and other flows in the ionosphere, (ii) to investigate their morphology and establish parameter requirements for their generation by possible magnetospheric drivers, and (iii) to identify possible common physics behind various flows in the ionosphere. Special attention will be devoted to the spectra of turbulence resulting from the instability and structure formation.

We shall primarily pursue a numerical approach in this investigation. Specifically, we will employ a system of fluid equations similar to those used in describing the DW-ZF turbulence, as, e.g., the Hasegawa-Wakatani (HW) system (Hasegawa & Wakatani, 1987) in magnetic fusion energy research and geostrophic flows. Together with its earlier subset, known as the Charney-Hasegawa-Mima model, the HW model has been broadly used for more than four decades in studying DW turbulence in plasmas and Rossby waves in atmospheric and oceanic dynamics.

At first, however, we provide a modified system to better suit the ionospheric conditions and lay the ground for future model development. In addition to the electrostatic potential and particle density operative for the zonal flow generation in the HW model, we include the parallel flow velocity and plasma pressure. While manifesting their subdominant role for this study, in that they can be calculated when the density and flow potential are obtained, they can be straightforwardly included in the code self-consistently, which we plan to do in the next model iteration. These fields are essential in connecting the ionosphere with the magnetospheric driver.

The paper is organized as follows. The HW model is introduced in the next section, and relevant aspects of its derivations are briefly discussed. In Sec.3, the linear stability analysis using a simple WKB-type approach is carried out. Sec.4 describes the simulation setup. The simulation results are presented in Sec.5 in two separate categories. The first set of simulations was executed using a symmetric density trough as an initial condition. While these results are limited to narrow troughs, the second category deals with the relaxation of a single-density wall. The results of these studies shed extra light on the relaxation of arbitrarily wide troughs and other ionospheric structures with sharp unidirectional density gradients. The paper closes with a summary and discussion of the results.

2 Model Equations

We describe the plasma dynamics using gyro-fluid type equations with resistivity in the plasma motion parallel to the magnetic field. We start by extending the HW (Hasegawa & Wakatani, 1987) two-field system of equations for the plasma density and electrostatic potential. The extended system also evolves the plasma pressure and the ion velocity component along the magnetic field. Depending on the spectrum extension to large wave numbers studied in this paper, we will also include finite Larmor radius (FLR) effects using the gyro-fluid methodology in the next version of this model.

The underlying idea behind the derivation of the HW model is to use the quasineutrality condition and to connect the density and potential perturbations, in the form $\nabla \cdot j = 0$. They also utilize the so-called "diamagnetic cancellations" between the FLR momentum heat flows and the diamagnetic velocity fluxes (e.g., Hinton & Horton, 1971), after obtaining the flow velocity from a drift approximation. In terms of the ordering, the fields are decomposed in a usual manner, as, e.g., for the density $n = n_0+n'$, with $n' \ll n_0$ but $\nabla n' \sim \nabla n_0$. Keeping the above in mind, we adhere to a more formal but systematic approach, starting from the Braginsky system (Braginskii, 1965).

The primary particle motion occurs in the forms of the ExB and diamagnetic drifts

$$\mathbf{V}_E = \frac{c}{B^2}\mathbf{B}\times\nabla\Phi, \qquad \mathbf{V}_{\mathrm{di}} = \frac{c}{enB^2}\mathbf{B}\times\nabla P_{\mathrm{i}}. \tag{1}$$

Here Φ is the full electrostatic potential, and P_i is the ion pressure. *In intense SAID channels, the electron temperature typically exceeds ion temperature by a factor of 3-5 at heights above 300* km, *while the ion temperature dominate at lower altitudes*(e.g., Liang et al., 2021, 2022; E. V. Mishin & Streltsov, 2024). In this paper, we will evolve only the density profile and keep the temperature profiles of both species fixed.

The velocity components in eq.(1) are largely incompressible and do not provide evolution when inserted in the quasineutrality, $\nabla\cdot\mathbf{j} = 0$, equation. We, therefore, need to add the ion polarization drift to V_{di}:

$$\mathbf{V}_{\mathrm{p}} = -\frac{c^2 M}{eB^2}\left[\frac{\partial}{\partial t} + (\mathbf{V}_E + \mathbf{V}_{\mathrm{di}})\cdot\nabla\right]\nabla\Phi$$

Using these expressions, including the diamagnetic cancellations mentioned above, the continuity equation for ions, their parallel velocity $V_\|$, and thermal balance equations can be written as follows (e.g., Horton, 1990):

$$\frac{\partial n_{\mathrm{i}}}{\partial t} + \mathbf{V}_E\cdot\nabla n_{\mathrm{i}} + \nabla_\perp\cdot(n_{\mathrm{i}}\mathbf{V}_{\mathrm{p}}) + \frac{\partial}{\partial z}n_{\mathrm{i}}V_\| = 0 \tag{2}$$

$$\frac{\partial V_\|}{\partial t} + \mathbf{V}_E\cdot\nabla V_\| + V_\|\frac{\partial V_\|}{\partial z} = -\frac{e}{M}\frac{\partial\Phi}{\partial z} - \frac{1}{Mn}\frac{\partial P_{\mathrm{i}}}{\partial z} - \nu_{\mathrm{in}}V_\| \tag{3}$$

$$\frac{\partial P_{\mathrm{i}}}{\partial t} + \mathbf{V}_E\cdot\nabla P_{\mathrm{i}} + V_\|\frac{\partial P_{\mathrm{i}}}{\partial z} + \gamma P_{\mathrm{i}}\frac{\partial V_\|}{\partial z} = 0 \tag{4}$$

where γ is the ion adiabatic index, which can be fixed, e.g., at $\gamma = 5/3$, $P_{\mathrm{i}} = nT_{\mathrm{i}}$, ν_{in} is the ion-neutral collision frequency, with other notation being standard. We have dropped small particle and heat diffusivity terms, along with the molecular viscosity term. These are expected to be predominantly turbulent, thus implicitly present in the above system. However, we will use small dissipative terms for regularization purposes in computations. After dropping some nonessential nonlinear terms discussed, e.g., in (Horton, 1990), eq.(2) rewrites

$$\frac{\partial n_{\mathrm{i}}}{\partial t} + \frac{c}{B}[\Phi, n_{\mathrm{i}}] + \frac{c^2M}{eB^2}\left(-n_0\frac{\partial}{\partial t}\Delta_\perp\Phi - \frac{c}{B}n_0[\Phi,\Delta_\perp\Phi] - \frac{c}{eB}[P_{\mathrm{i}},\Delta_\perp\Phi]\right) + \frac{\partial}{\partial z}n_{\mathrm{i}}V_\| = 0$$

We have introduced the Poisson bracket as

$$[f,g] = \frac{\partial f}{\partial x}\frac{\partial g}{\partial y} - \frac{\partial f}{\partial y}\frac{\partial g}{\partial x}$$

Next, using the quasineutrality condition, $n_{\mathrm{e}} = n_{\mathrm{i}} = n$, and the electron continuity equation within the guiding center approximation in eqs.(1),

$$\frac{\partial n_{\mathrm{e}}}{\partial t} + \frac{c}{B}[\Phi, n_{\mathrm{e}}] + \nabla_\| n_{\mathrm{e}}V_{\mathrm{e}\|} = 0, \tag{5}$$

where $V_{e\parallel}$ is the parallel electron velocity, we relate the density and potential perturbation as follows

$$\frac{c^2M}{B^2}\left(n_0\frac{\partial}{\partial t}\Delta_\perp\Phi+\frac{c}{B}n_0\left[\Phi,\Delta_\perp\Phi\right]+\frac{c}{eB}\left[P_i,\Delta_\perp\Phi\right]\right)-\nabla_\parallel\cdot\mathbf{j}=0 \tag{6}$$

Here, $j_\parallel$ can be straightforwardly related to P and Φ from the electron momentum balance:

$$j_\parallel=\frac{e}{m\nu_{\mathrm{ei}}}\left(\nabla_\parallel P_{\mathrm{e}}-en_{\mathrm{e}}\nabla_\parallel\Phi\right)$$

Using the last three relations, we rewrite eqs.(5) and (6) as follows:

$$\frac{\partial n}{\partial t}+\frac{c}{B}\left[\Phi,n\right]-\frac{1}{m\nu_{\mathrm{ei}}}\left(\nabla_\parallel^2P_{\mathrm{e}}-en_0\nabla_\parallel^2\Phi\right)=0$$

$$\frac{\partial}{\partial t}\Delta_\perp\Phi+\frac{c}{B}\left[\Phi,\Delta_\perp\Phi\right]+\frac{c}{eBn_0}\left[P_{\mathrm{i}},\Delta_\perp\Phi\right]-\frac{M\omega_{\mathrm{ci}}^2}{m\nu_{\mathrm{ei}}en_0}\left(\nabla_\parallel^2P_{\mathrm{e}}-en_0\nabla_\parallel^2\Phi\right)=0, \tag{7}$$

where ω_{ci} is the ion Larmor frequency and ν_{ei} is the electron-ion collision frequency. We have not included collisions with neutrals in the friction force acting on electrons, assuming that the $\nu_{\mathrm{en}}/\omega_{\mathrm{ce}}$ is very small, *which is a valid assumtion in the top ionosphere.* The ionospheric flows of our interest often have a stronger density inhomogeneity than that of the temperature by almost an order of magnitude. Under these conditions, the above two equations form a closed system if we approximate the pressure as $P_{\mathrm{e,i}}=T_{\mathrm{e,i}}n$, assuming the base temperature profile $T=T_0\left(y\right)$ (but not the density) being fixed, where y is the latitude. Note, however, that we call y latitude and x longitude here and below just for simplicity. A more accurate definition of these coordinates is that y is aligned with the density gradient, x is aligned with the constant density surface, and z is in the magnetic field direction. In real geometry, especially in equatorial regions, this coordinate system may be turned around the magnetic field and misaligned with longitude and altitude.

One advantage of neglecting the temperature variations is the similarity of this case with a well-studied HW (Hasegawa & Wakatani, 1987) model of the DW turbulence. This model assumes cold ions, so the third term in eq.(7) is absent. We keep it for assessing its impact on the linear instability but will drop it for simplicity when performing the simulations. Introducing the following dimensionless variables

$$\omega_{ci}t\to t;\quad x,y,z/\rho_s\to x,y,z;$$

where $\rho_{\mathrm{s}}=\sqrt{T_{00}/M}\omega_{\mathrm{ci}}^{-1}$, with T_{00} being the fiducial electron temperature, as is the density n_{00} introduced below, we relate them to one of the y- ends of the (x,y) integration box. Depending on the particular simulation setup, these quantities may be the same or different at the endpoints. Here, we adopt a geophysical convention of the equilibrium gradients pointing to y rather than x (as in plasma literature) direction. Using the above notation, we arrive at the HW equations, supplemented by the ion pressure term. We will also normalize the dependent variables $e\Phi/T_{00}\to\Phi$, $n/n_{00}\to n$. The term stemming from the ion pressure $P=P_{\mathrm{i}}/n_{00}T_{00}$ will be used only for the linear instability. The dimensionless equations then read:

$$\frac{\partial}{\partial t}\Delta_\perp\Phi+\left[\Phi+P,\Delta_\perp\Phi\right]+\alpha\left(\tilde{n}-\tilde{\Phi}\right)=0 \tag{8}$$

$$\frac{\partial n}{\partial t}+\left[\Phi,n\right]+\alpha\left(\tilde{n}-\tilde{\Phi}\right)=0 \tag{9}$$

We have also subtracted the zonal averaged, $\langle\cdot\rangle$, quantities in the terms under the $\nabla_{\|}$ -operator by introducing

$$\tilde{n} = n - \langle n \rangle, \quad \tilde{\Phi} = \Phi - \langle \Phi \rangle$$

and replacing

$$\alpha = -\frac{V_{\mathrm{Te}}^2}{\nu_{\mathrm{ei}}\omega_{\mathrm{ci}}}\nabla_{\|}^2 \to \frac{k_{\|}^2 V_{\mathrm{Te}}^2}{\nu_{\mathrm{ei}}\omega_{\mathrm{ci}}}.$$

Subtracting $\langle n \rangle$ and $\langle \Phi \rangle$ from n and Φ in the last terms of the above equations is justified in the magnetic plasma confinement contexts by the magnetic field shear that mixes the zonally averaged variations of the respective quantities. In the SAPS applications, this modification can be justified by a strong shear in the vertical velocity $V_{\|}(y)$ (Huang et al., 2007). As the magnetic shear in Tokamaks, this effect does not enter the HW system explicitly, but it should also be taken into account in calculating the electron response.

Under zonally-averaged quantities, we understand averaging along the homogeneous direction of the problem (i.e., longitude, x) while the quasi-stationary variations of n and Φ are in y-direction. It is assumed that $\nabla_{\|}\langle\tilde{\cdot}\rangle \equiv 0$. The rationale behind this assumption is that the zonally-averaged perturbations vary much slower in time than $\tilde{n}$ and $\tilde{\Phi}$ and, therefore, they spread along the field during the time so that their variation in this direction is much smoother: $\nabla_{\|}\langle n \rangle, \nabla_{\|}\langle \Phi \rangle \ll \nabla_{\|}\tilde{n}, \nabla_{\|}\tilde{\Phi}$. The simplification associated with the replacement of the $\nabla_{\|}$- operator by a constant can be justified, assuming that the perturbations $\tilde{n}$ and $\tilde{\Phi}$ vary in z- direction as $\exp\left(ik_{\|}z\right)$ and there exists a maximum growth rate in $k_{\|}$, thus defining α, which we confirm in the next section. While making this extension to the third dimension in the ambient magnetic field direction, we simplify the dynamics across it by neglecting temperature and magnetic field gradients. Their contribution to the dynamics, including a gravity effect of magnetic field curvature has been investigated in conjunction with the flute mode generation in the ionosphere (Sotnikov et al., 2008; V. Sotnikov et al., 2014). For similar reasons, the vertical velocity $V_{\|}$ is considered subdominant relative to the main n and Φ variables, and we do not evolve $V_{\|}$ in this simple version of the HW model. It can be obtained *a posteriori* from eq.(3) using Φ obtained from the main model eqs.(8-9). Next, we examine the linear stability of our model.

3 Linear Instability

In this section, we perform a linear stability analysis of eqs.(8-9) using a simple short-wave approximation. Namely, we consider the following instability driving parameters, associated with the density and pressure gradients as constants, along with the adiabaticity parameter α, introduced earlier:

$$\kappa = \frac{1}{n_0 T_{0\mathrm{e}}}\frac{\partial}{\partial y} n_0 T_{0\mathrm{i}} \approx const, \qquad \beta = \frac{1}{n_0}\frac{\partial}{\partial y} n_0 \approx const,$$

Here the zonal averaged profiles $T_0(y)$ and $n_0(y)$ are also normalized to T_{00} and n_{00}. Linearizing then eqs.(8-9) with respect to $\tilde{n}$ and $\tilde{\Phi}$, we obtain

$$\frac{\partial}{\partial t}\Delta_{\perp}\tilde{\Phi} - \kappa\Delta_{\perp}\tilde{\Phi}_x + \alpha\left(\tilde{n} - \tilde{\Phi}\right) = 0$$

$$\frac{\partial \tilde{n}}{\partial t} + \beta\tilde{\Phi}_x + \alpha\left(\tilde{n} - \tilde{\Phi}\right) = 0$$

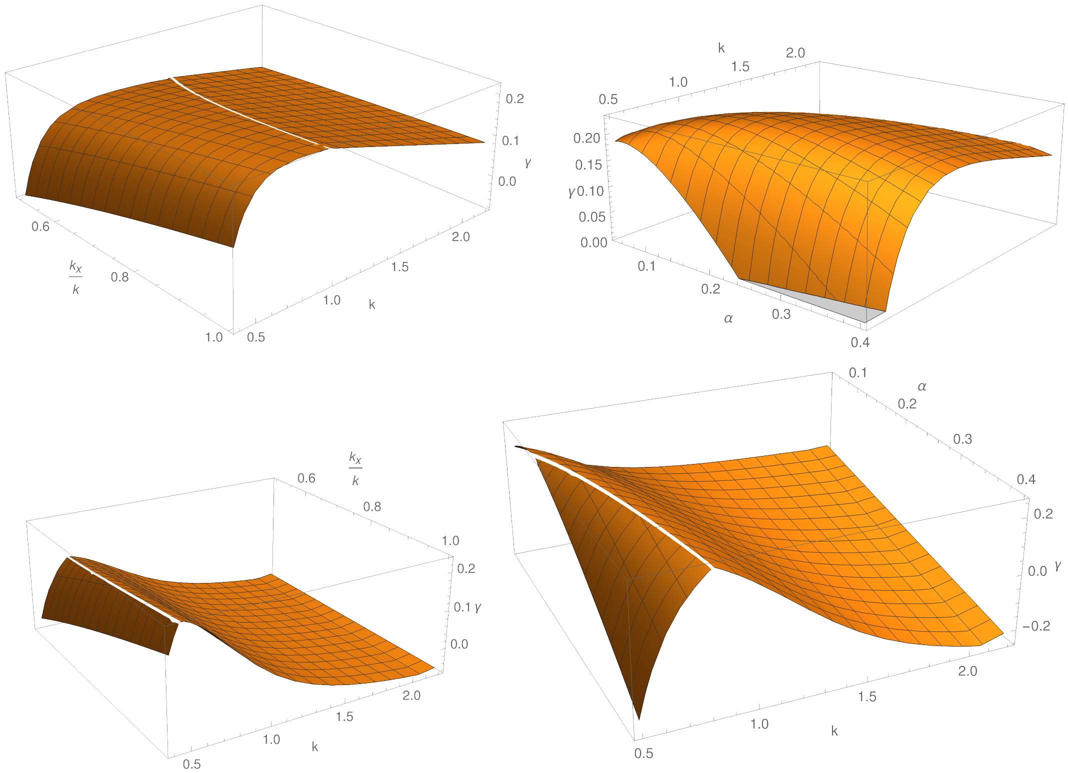

Figure 2. **Left upper panel**: Instability growth rate as a function of wave number k and k_x - its components across plasma gradients and magnetic field, computed for $\alpha = 0.1$. **Right upper panel**: Growth rate shown as a function of k and α, for $k_x = k$. The remaining parameters in eq.(10) are fixed at $\beta = 2$, $\kappa = 0.2$. **Lower panels** The same as upper panels but for $\kappa = 1.2$. White lines on the surfaces mark a change of the square root branch in eq.(11) where the denominator of the expression under $\tan^{-1}$ crosses zero.

Using the last two equations, we derive the following dispersion equation for the perturbations of the form $\exp\left(-i\omega t + ik_x x + ik_y y\right)$

$$\omega^2 + \left[\kappa k_x + i\alpha\left(k^{-2}+1\right)\right]\omega + i\alpha k_x\left(\kappa - \beta k^{-2}\right) = 0 \tag{10}$$

The two roots for the frequency ω can be written as

$$\omega = -i\alpha\left(1+k^{-2}\right) - \kappa k_x \pm \sqrt{\kappa^2 k_x^2 - \alpha^2\left(1+k^{-2}\right)^2 + \frac{2i\alpha k_x\left(2\beta+\kappa-\kappa k^2\right)}{k^2}}, \tag{11}$$

while the growth rate

$$\gamma = \Im\omega = -\alpha\left(1+k^{-2}\right) + \sqrt{r}\left|\sin\frac{\vartheta}{2}\right|,$$

where

$$r = \sqrt{\left(\kappa^2 k_x^2 - \frac{\alpha^2\left(k^2+1\right)^2}{k^4}\right)^2 + \left(\frac{2\alpha k_x\left(2\beta+\kappa-\kappa k^2\right)}{k^2}\right)^2},$$

$$\theta = \tan^{-1}\left[\frac{2\alpha k^2 k_x\left(2\beta+\kappa-\kappa k^2\right)}{\kappa^2 k^4 k_x^2-\alpha^2\left(k^2+1\right)^2}\right]$$

This solution is shown in Fig.2 in two different representations for fixed values of parameters $\beta = 2$ and two values of $\kappa = 0.2$ and $\kappa = 1.2$. In the latter case, the excitation zone is narrower and at lower values of k than in the former case. Note that smaller values of $\kappa \ll \beta$ correspond to a temperature gradient being as strong but opposite to the density gradient. This equilibrium corresponds to a pressure-balanced structure across the magnetic field, $nT \approx const$, whereas the case $\kappa \approx \beta$ corresponds to the case of constant temperature. It is also worth mentioning that the growth rate maximizes at $k_x \approx k$, and it also has a broad maximum in $\alpha \sim 1$, which selects a range of most unstable waves in k_z. This is another justification of a single adiabaticity parameter α, introduced in the previous section.

The above instability analysis is oversimplified where the $y-$ scale of perturbations is not much shorter than the domain size as it does not adequately describe the eigenfunctions of the density and potential perturbations. Nevertheless, it is useful as a guidance tool to select appropriate parameter values for simulations that we describe in the next section.

4 Simulation Setup

We perform our simulations in a channel box that is periodic in x- direction ("longitude") and has rigid boundaries in y direction ("latitude", see text below eq.[7]). This choice of simulation geometry reflects a density trough morphology, discussed in the Introduction. Given the computational limitations on the spatial scales, we have split the simulations into two complementary sets. The first set addresses the sustainability of an entire density trough against turbulent transport generated by gradient-driven instabilities, developing primarily at its walls. Within this setting, the edge density is maintained at the same level on both sides of the trough. The rate at which the influx of the outer plasma refills the trough will quantify the efficiency of transport regulation by generated ZFs.

Due to the vast difference in scales between a typical density trough latitudinal profile and gradient-driven turbulence, the above-described simulation setup cannot adequately address the formation and sustainability of a well-pronounced density trough. In other words, the above full-trough simulation setup can capture only narrow troughs and, thereby, relatively shallow ones with a density contrast, say, $\Delta n \lesssim 10$. Although these studies are of significant interest, many troughs are at least a few degrees in latitude. The question of our results' scalability for the narrow troughs arises. Moreover, our goal is to link the macroscopic trough sustainability to microturbulence excited at its walls. If not self-regulated or otherwise suppressed, the turbulence would lead to a rapid refill of the trough. However, to investigate how microturbulence generates mesoscale ZFs in full-size density troughs would be computationally very expensive.

To alleviate this problem, the second set of simulations will be employed. It zooms in the area of a sharp density gradient at one of the two walls of the trough. This setup is motivated by observations of troughs having step-like walls that, as it seems, do not interact with each other. We simulate an isolated wall by using an adjacent flat bottom and top of the density profile as boundary conditions (BC). Such structures are often observed (cf. Fig.1). In this setting, much fewer computational resources must be invested, as it focuses on a steep part of the density profile that does not spread significantly in the flat areas.

Based on the above considerations, the boundary condition in the second simulation is set to maintain a fixed density contrast between the y- boundaries of the box, starting from a step-like density distribution. In this case, particle flux initially drives the turbulence where the gradient is sufficiently large. This setup is suitable for demonstrating a mesoscale character of zonal flow generation and flux suppression. It provides a necessary link between microturbulence and the full-scale density trough phenomenon.

Returning to the full-trough simulation, we will start it from an inverted bell-shaped density profile. Morphologically, it corresponds to a trough event, shown, e.g., in Fig.1 of (Foster & Burke, 2002) between $50-54°$ longitude, but much narrower in longitude. Indeed, other data show local density variation in the troughs over scales less than $0.5°$ (Huang et al., 2007), which are often unresolved, e.g., Fig.1, at latitudes $-41°$ and $-59°$. We set periodic BC in x- direction, $n\left(x+L_x, y, t\right)=n\left(x, y, t\right)$ and apply the same condition for Φ. In two sets of simulations, we will use boundary conditions with and without density contrast across the channel for the step-like and trough-like initial density profiles. The stream function, $\Phi=0$ at $y=0, L_y$. We start with a symmetric trough with equal density values at the edges and a minimum in the middle. At $t=0$ a random noise of weak fluctuations is added to this density profile. The initial potential, Φ, contains only a weak random noise.

It should be noted, however, that most of the past numerical studies of systems similar to eqs.(8-9) have been carried out in a flux-driven, doubly-periodic simulation box. To model the relaxation of a density trough imposed as an initial condition, it is more appropriate to apply the periodicity condition only across the plasma gradient. Apart from a background density profile, the initial conditions are given by statistically isotropic, random perturbations suppressed toward large wave numbers. The hyperviscosity/hyperdiffusivity coefficients (standard for the spectral codes, not shown in eqs.[8-9] for clarity) are applied to suppress the “spill over” of higher harmonics.

The most runs presented in this paper were performed on a grid with $N_x \times N_y$ =512x512 spatial points. However, they have been verified using limited runs on 512×1024 grids, which we also used for studies of fluctuation Fourier spectra. Given that the typical spectra obtained from simulations, e.g., those presented in Sec.5.6 are very steep, the code resolution is sufficient for the phenomena studied. Mode de-aliasing is achieved by truncating the number of modes at approximately $N_{x,y}/3$. For example, we truncate the spectrum at 160x320 Fourier harmonics for the finest resolution choice indicated above.

We have solved the system in eq.(8-9) using appropriate Fourier decompositions. According to the Dirichlet boundary condition across the channel between $y=0, L_y$, a mere sine expansion suffices for the y-direction. The $y-$dependent background density profile enters the equation only as a product with the plasma potential that vanishes at both y boundaries. Therefore, an additional cosine expansion is not needed. We utilize the spectral library ISPACK, documented in, e.g., `http://www.gfd-dennou.org/library/spmodel/#label-2`. The time-stepping is based on the second-order explicit Adams–Bashforth algorithm.

5 Simulation Results

Before turning to the simulation results, discussing their scalability concerning the box size and the density contrast imposed as a boundary and initial condition is worthwhile. Because of computational constraints, we cannot change these parameters at will as a sizable rescaling exerts much stress on the code, thus increasing the computation costs. In addition, we will precede our presentation of simulation results by a brief subsection of their outcome.

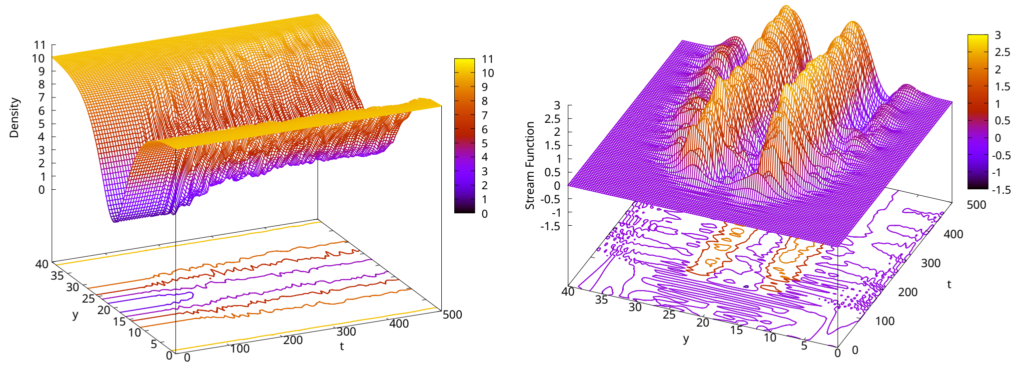

Figure 3. Time evolution of the density and potential averaged in zonal direction (x, periodic coordinate). The initial density profile is set to a V-shaped plasma depletion with a minimum at the middle of the trough, where the density $n_0 = 1$. The density is maintained at $n_1 = 10$ at both edges of the trough. The adiabaticity parameter $\alpha = 1.5$.

5.1 Scalability Issues

Even the simplest version of eqs.(8-9) with $P = 0$ does not allow us to rescale a given simulation result to larger boxes without rerunning the code. Indeed, by rescaling coordinates, time, and dependent variables as $x, y, t \to \lambda x, \lambda y, \tau t$ and $\Phi \to \left(\lambda^2/\tau\right)\Phi$, $n \to \left(\lambda^2/\tau\right) n$, respectively, we arrive at the following system

$$\frac{\partial}{\partial t}\Delta_\perp \Phi + [\Phi, \Delta_\perp \Phi] + \lambda^2 \tau \alpha \left(\tilde{n} - \tilde{\Phi}\right) = 0 \tag{12}$$

$$\frac{\partial n}{\partial t} + [\Phi, n] + \tau\alpha\left(\tilde{n} - \tilde{\Phi}\right) = 0 \tag{13}$$

We have chosen the λ^2/τ scaling factor to keep the convective parts of equations invariant. We also limit our discussion to the case of an equal box transformation in both directions by the same factor λ.

Assume that we have performed a system scan in α using our code for $\lambda = \tau = 1$. However, mapping $\tau\alpha \to \alpha$, for $\tau \neq 1$ does not make the system invariant to the above scale transformations. Since we originally normalized the spatial scale to the ion sound Larmor radius, ρ_s, which is relatively small for the processes at hand, our interest is to increase the box size, that is, to get a handle on the case $\lambda \ll 1$. Therefore, any result obtained before rescaling, that is, for $\lambda = \tau = 1$ cannot be mapped to the system behavior in significantly larger boxes, even if we ignore the additional problems associated with the insufficient short-scale resolution that arise from the box stretching without mesh refinement. As seen from the above equations, for $\lambda \ll 1$ the density perturbations are subdominant to the potential and convected with the flow almost as a passive scalar. Note that stretching of the spatial variable generally reduces the growth rate, but increasing τ does not alleviate the problem of the system's bias in favor of Φ. These considerations will help us choose the simulation parameters and plan for the next steps. A simple way to restore the role of Φ in the dynamical feedback loop of the system is to reinstate the ion pressure, P, in the equation for Φ that we dropped in eq.(12). We defer these results to a future report.

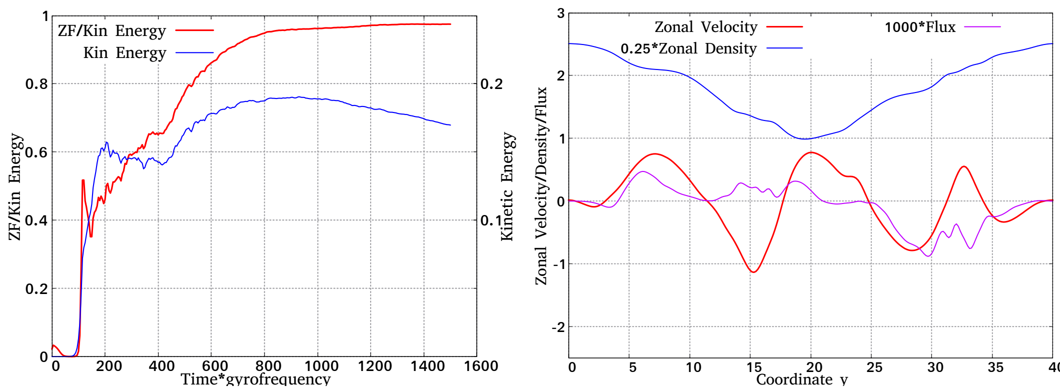

Figure 4. Left panel: Time evolution of the ratio of the box-averaged ZF kinetic energy to the full kinetic energy (red) and kinetic energy (blue). Right panel: Zonally-averaged (over x) profiles of density, velocity, and turbulent flux in y-direction at $t = 1500$, when most of the plasma kinetic energy is in the ZF component. Other simulation parameters, IC and BC, are the same as in Fig.3.

5.2 Expected Simulation Outcome

Notwithstanding the above limitations, the two-field model given by eqs.(8-9) and discussed in Sec.2 captures distinctively different turbulence and transport scenarios, including those described in the Introduction. Extensive studies of similar systems carried out primarily in the areas of magnetic fusion energy research and geostrophic flows can be distilled to two different transport regimes. An initially unstable plasma profile can relax to either of them by a turbulent transport, unstably driven by the plasma density or temperature gradients. However, the depth of the plasma relaxation will be markedly different in these regimes.

The first regime is characterized by strong-turbulence transport, driven by the DW instability. It leads to flattening the initially unstable density or temperature profile to a marginally stable one with strong residual turbulence and associated transport. The second regime evolves through a phase of self-organization of excited turbulence. Most of its energy is channeled into zonal flows that suppress the turbulence level and particle transport while the initially strong density gradient persists or suffers only a moderate flattening.

In distinguishing between these two regimes, there is no significant difference in whether the instability is driven by temperature and density gradient or just one of them. We, therefore, limit our study to a straightforward case in which the density gradient drives the instability, whereas the ion pressure is neglected compared to the electron pressure. The latter enters the equations through the normalization of Φ and the adiabaticity parameter α. Since only subdominant plasma temperature variations are typically observed in density troughs, we impose the condition $P = 0$ in eq.(8). This reduces the number of instability control parameters from three to two, as we set $\kappa = 0$ in the instability analysis presented in Sec.3. According to this analysis, the ion pressure gradient has no profound effect on the instability growth rate.

At the same time, omitting the ion pressure greatly simplifies the energetics of the system at hand. Indeed, we can define the total energy as follows:

$$E_{\text{tot}} \equiv \frac{1}{2} \int \int \left[|\nabla \Phi|^2 + (n - \eta)^2 \right] dxdy, \tag{14}$$

where η is an arbitrary constant. This constant can be introduced because eqs.(8-9) are invariant against the replacement $n \to n + const$. Meanwhile, $E_{\rm tot}$ strictly decreases with time:

$$\frac{dE_{\rm tot}}{dt} = -\alpha \int\int \left(\tilde{\Phi} - \tilde{n}\right)^2 dxdy$$

As indicated earlier, we start the simulation with a weak noise of $\tilde{\Phi}$ and $\tilde{n}$, and a density profile $n(0,y) = n_0(y)$, with a typically high density contrast across the channel, $n_{\rm max} \gg n_{\rm min}$. The flow potential can thus grow significantly only if the instability decreases the box-averaged value of $(n-\eta)^2$. Since at $t = 0$, $\Phi \approx 0$, the most informative choice of η with regard to the grows of $|\nabla\Phi|^2$, is to minimize the second term under the integral in eq.(14). This requirement leads to $\eta = \overline{n_0}$, where the bar denotes an averaged value over the interval $0 < y < L_y$.

Another integral quantity that constrains the energy pathways of the system is based on the conservation of any arbitrary function, F, of the potential vorticity, $w = \Delta\Phi - n$:

$$\frac{d}{dt}\int\int F(w)\, dxdy = 0$$

For example, we can use the enstrophy

$$\mathcal{E} = \frac{1}{2}\int\int (\Delta\Phi - n)^2 dxdy = const,$$

to control the code accuracy.

5.3 Transport Barriers in Density Troughs

To understand the density profile evolution in a trough, which undergoes unstable growth of DWs presumably driven at its walls, we set the following initial conditions in a box $(0,0,L_x,L_y)$. To mimic a simple symmetric trough profile, the simulation starts with a V-shaped latitudinal density distribution of the form

$$n(y) = n_1 - \frac{n_2}{\cosh\left(\frac{y - L_y/2}{L_y\delta}\right)},$$

and zero mean potential. Both quantities are, however, superposed by small-amplitude random fluctuations added as Fourier harmonics with random phases and amplitudes. To accelerate the initial phase of the system evolution, we suppress the random harmonics exponentially toward the highest wave numbers. The above density profile typically stays frozen, and the plasma potential fluctuations do not grow above the initial noise level for the first tens of time units ($\omega_{\rm ci}^{-1}$). After the most unstable modes grow to amplitudes sufficient to produce significant anomalous diffusion, the density profile starts rapidly flattening. However, in the case of $\alpha \sim 1$, the ZF also grows so that the density flattening stops because of the backreaction from the ZF. If the established ZF is strong, the zonally-averaged (in x direction) density profile freezes again, apart from its turbulent fluctuations around the mean value.

An example of the density trough relaxation outlined above is shown in Fig.3. During the first 50-100 time units, the gradient-driven instability grows sufficiently for the turbulent diffusion to refill the bottom of the density trough. The refill material is supplied from the steep parts of the initial density profile where the instability is the strongest. The areas adjacent to the edges of the trough remain undisturbed since the density gradient there is subcritical regarding the instability. This behavior is consistent with the instability analysis in Sec.3. The surface plots show that the turbulence, time-averaged zonal density, and potential profiles rapidly spread toward the trough edges. Had they proceeded at the same pace, the relaxed part of the density profile would have reached the trough edges in a few tens of time units. Instead, the system comes to a quasi-stationary state after $t \approx 200$, so the relaxation front does not reach the edges. The density gradient relaxation proceeds further for smaller $\alpha \ll 1$, which we will consider in the next section by focusing on one wall of a trough.

Time-asymptotic profiles of zonally-averaged density, velocity, and a strongly suppressed particle flux are shown in the right panel of Fig.4 for the case considered above. Comparing the left panel with Fig.3, we see that the fast density relaxation ceases when the ZF absorbs a significant part of the system's kinetic energy. As the wave amplitudes are not growing and even a slow decay of the plasma kinetic energy is evident from Fig.4, the density profile remains steep enough to produce linear instability. However, its growth is suppressed by the excited ZF. Apart from arresting the growth of wave amplitudes, it slows down turbulent transport. The area of its suppression extends toward the trough edges, where the plasma is locally stable. This configuration fully preserves the trough from edge erosion, thus maintaining the integral plasma depletion indefinitely within the integration time. Again, such a relaxation outcome is impossible for significantly smaller adiabaticity parameter α values.

Now, we briefly consider the role of plasma parameters in selecting the trough relaxation scenario. We reduced the number of control parameters to two, of which β controls the initial instability growth, but the evolving density profile then takes over its role. As we emphasized, the adiabaticity parameter, α, is more critical for the regime selection. The observed turbulent transport barriers are formed for $\alpha \approx 1$. For $\alpha \ll 1$, the transport barriers do not emerge or are weak, so the wall erosion proceeds to the trough edges. Projecting this situation on a real trough, we may predict that it will be broadened and refilled with the external plasma if $\alpha \ll 1$. Again, we do not include the field-aligned transport here, which may be ineffective in filling the trough regardless of our model limitations (e.g., Huang et al., 2007). To investigate a trough relaxation in more detail, in the next Section we focus on one particular wall of the trough, as the overall picture of the full trough is mainly symmetric.

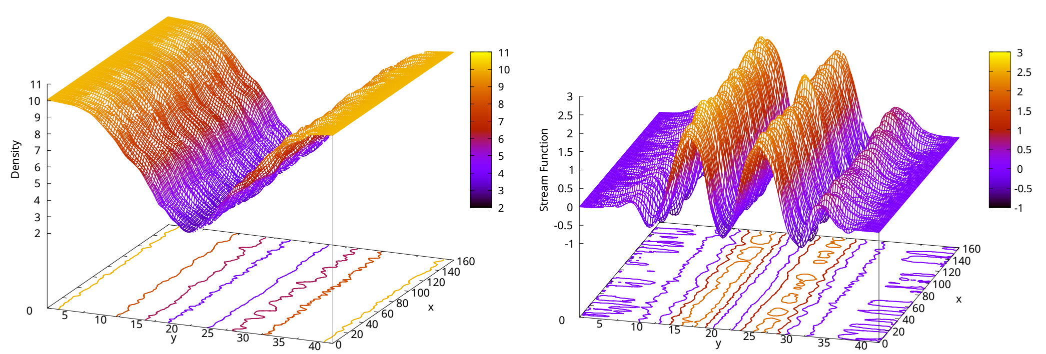

Figure 5. Time-asymptotic distribution of the density (left panel) and plasma potential (right panel) at $t = 500$. The simulation parameters, IC and BC, are the same as in Fig.3.

5.4 Sustainability of Density Walls

In this section, we study the density gradient relaxation in the DW-ZF turbulence by focusing on one of the walls of a density trough or any other structure where an isolated density jump is present. This approach allows us to gain more insight into the formation of transport barriers pertinent to broader and deeper troughs. The DW instability is expected to originate at the maximum density gradient. Numerous observations show that density depletions exceed two orders of magnitude (e.g., Huang et al., 2007), occurring over a $\sim 1^\circ$ latitudes. While the results of the previous section are formally applicable to narrow density troughs, by focusing on one of the walls, we can measure the transport barrier penetrability in *broader density structures.* The bottom of such troughs is often flat, but the walls are steep. Therefore, a step-like initial density profile should adequately describe the trough relaxation at either of its two walls. The imposition of the channel boundary conditions at $y = 0, L_y$ allows us to infer how far the relaxing part of the initial density profile may spread as the outer plasma percolates through the barrier to the bottom of the trough.

The initial density profile is then set in the form of a step,

$$n_0(y) = n_1 + \frac{n_2 - n_1}{\tanh\frac{L_y - a}{L_y\delta} + \tanh\frac{a}{L_y\delta}}\left(\tanh\frac{y-a}{L_y\delta} + \tanh\frac{a}{L_y\delta}\right),$$

raising from n_1 to n_2. Its raise, centered at $y = a$, is smoothed out by a *tanh* function over the scale $L_y\delta$. Compared to the full-trough relaxation presented in the preceding section, the wall relaxation more clearly reveals the fine structure of the relaxed density step. The “staircase” profile seen in Fig.6 forms, following a transition period. It lasts for several tenths of $\omega_{\mathrm{ci}}^{-1}$ after the onset of instability, during which the staircase fully develops and saturates. Staircase formation is not unusual in the turbulent transport phenomena in various settings (e.g., Balmforth et al., 1998; Dif-Pradalier et al., 2015; Dritschel & McIntyre, 2008; Guo et al., 2019; Y. J. Kim et al., 2022; Malkov & Diamond, 2019; Milovanov et al., 2021; Pružina et al., 2022) and references therein. The alternation of steep and flat pieces of the density profile mirrors variations in the anomalous plasma diffusivity. A noteworthy aspect of this profile is that the transport-driving turbulence is not significantly diminished after the relaxation is completed and the density profile freezes. The total plasma energy, eq.(14),

$$E_{\mathrm{tot}} \equiv \frac{1}{2}\int\int\left[\left|\nabla\Phi\right|^2 + \left(n - \overline{n}_0\right)^2\right]dxdy > \frac{1}{2}\int\int\left(\left|\nabla\Phi\right|^2 + \tilde{n}^2\right)dxdy \equiv E_{\mathrm{turb}} \qquad (15)$$

is not conserved by eqs.(8-9), cf. eq.(14). Since the simulation starts from $\Phi \approx 0$, the free energy for the DW instability is in the $\left(n - \overline{n}_0\right)^2$ term of the total energy. We included here the ZF energy into a turbulent component on the r.h.s. of the inequality above to show that the ZF taps energy from $\left(n - \overline{n}_0\right)^2$. The relaxation is similar to the one presented in the preceding section. It begins with an unstable growth of DWs that quickly saturates when a strong ZF establishes and the particle flux through the transport barrier drops precipitously.

5.5 Density Wall Thickening and Destruction

The simulation results reported in the preceding subsection have demonstrated a minimal density wall thickening after its relaxation in the case of adiabaticity parameter $\alpha \sim 1$ and the density contrast across the wall $\Delta n \sim 10$. Although the DW instability proved strong, and the ensuing anomalous diffusion typically starts dismantling the wall at a high pace, it slows down abruptly and seemingly comes to its end, e.g., Fig.6 (left panel), as soon as ZF streams arise. The resulting density profile acquires an appearance of a staircase, but the wall thickens by a mere factor of two or so. Given the narrowness of the observed density depletions (Huang et al., 2007), it might not even be detectable. The flux-stopping ZF becomes progressively more laminar toward the end of the relaxation and the plasma diffusive flux drops sharply from its initial burst observed at the outset of relaxation, Fig.7.

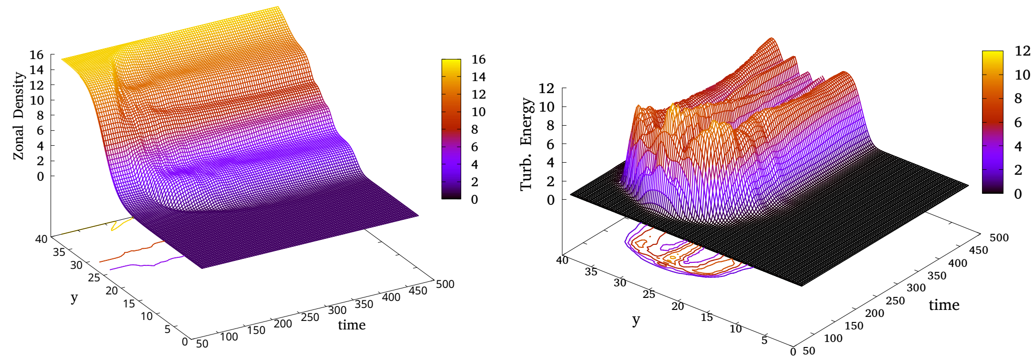

Figure 6. **Left panel:** Relaxation of a step-like initial density profile. **Right panel:** Time evolution of the turbulent energy profile, averaged only in x- direction, i.e., as a function of time and y (cf. eq.[15]). The simulation parameters are as follows: $n_1 = 1$, $n_2 = 15$, $\alpha = 1$.

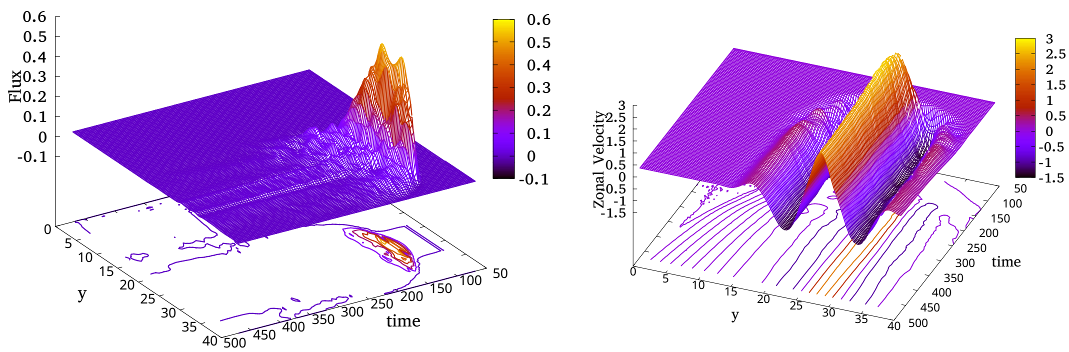

Figure 7. Same as in Fig.6 but for the diffusive particle flux $\left\langle \tilde{n}\tilde{V}_y \right\rangle$ and zonal velocity $\langle V_x \rangle$.

That said, the question to be posed is how far the system parameters can deviate from those above, in fact, optimal parameter values. In particular, one may ask whether the plasma diffuses far enough from the edge into the depleted density region, e.g., to refill a broad density trough. A thorough parameter scan is beyond the scope of this paper, mainly because such a scan should go deeper than scanning in α and Δn. As we discussed in Sec.5.1, a box resizing should make a significant impact on the result by effectively ascribing two different values to the parameter α: One is in the density, and another is in the vorticity equation. Here, we present the effect of changing α on the density wall sustainability and destruction.

We show in Fig.8 another simulation of turbulent relaxation in time of the same density wall as shown in Fig.6. However, this simulation was carried out for two smaller values of α, namely $\alpha = 0.1$ (left panel) and $\alpha = 0.03$ (right panel). The other parameters are the same as listed in Fig.6. It can be concluded from these three runs that the decrease of α leads to less efficient transport suppression. The same initial density profile attached to the high-density side of the channel broadens faster and reaches farther toward the opposite side for smaller α.

We also show in Fig. 8 the zonal flow profile, averaged along the channel, as a function of time. A close relation between the flux suppression efficiency and the ZF strength and regularity is seen from these plots. Note that for the smallest $\alpha = 0.03$, the ZF is

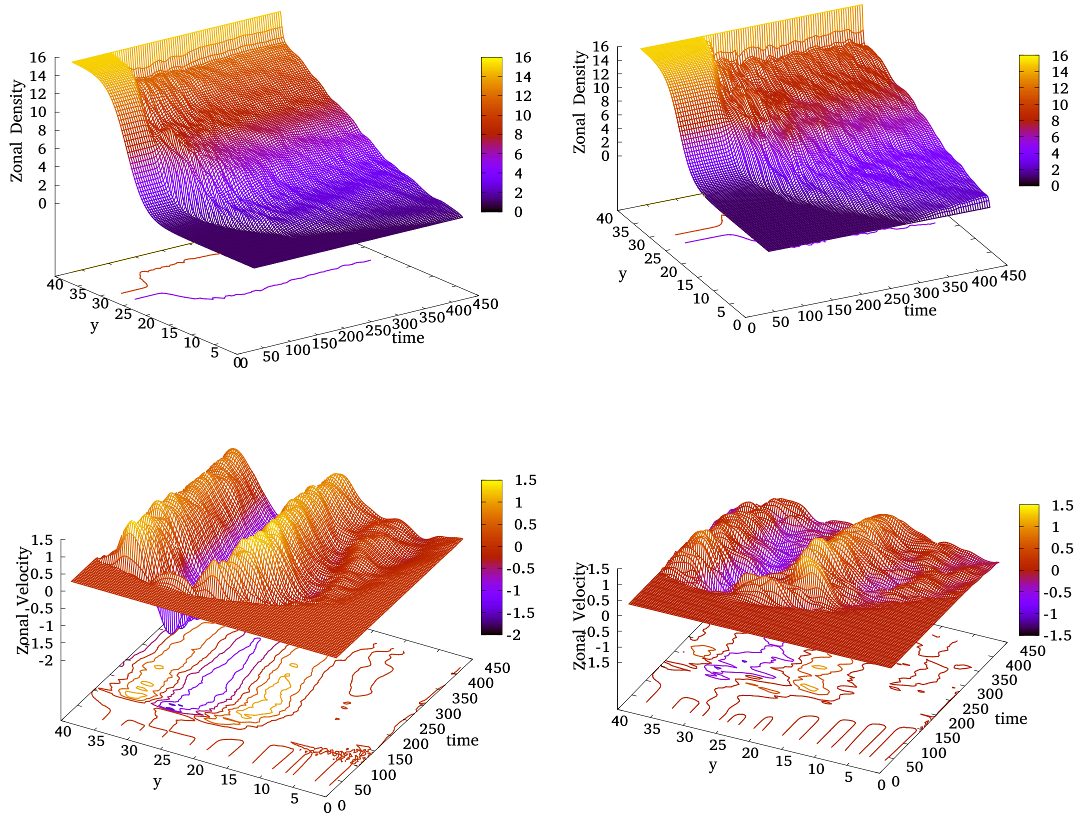

Figure 8. Density wall relaxation for two values of the adiabaticity parameter $\alpha = 0.1$ (left panel) and $\alpha = 0.03$ (right panel) to be compared with the density profile shown for the same values of other parameters in Fig.6 but for $\alpha = 1$.

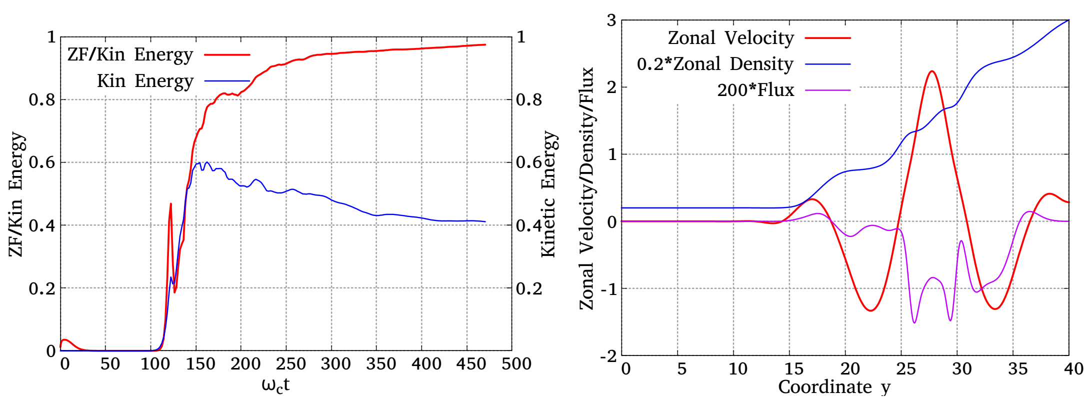

Figure 9. Same as Fig.4 but for wall simulation shown in Fig.6.

highly turbulent and relatively slow compared to the fast and laminar flow for $\alpha \approx 1$, shown in Fig.7.

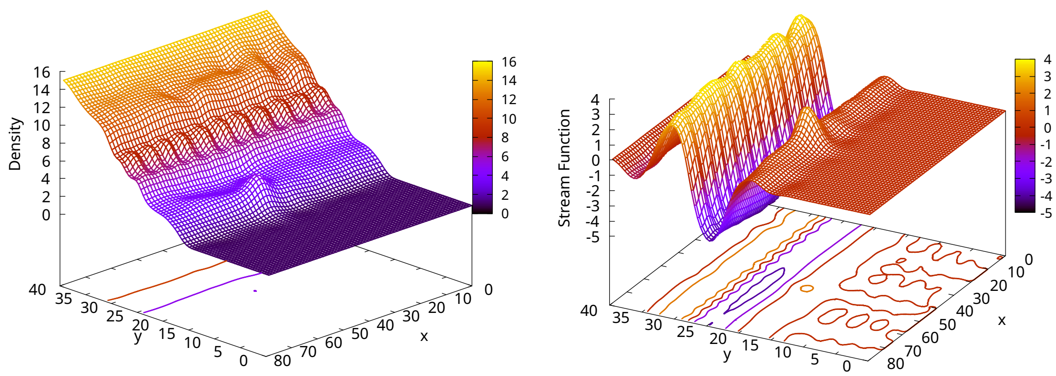

Figure 10. Same as in Fig.5 but for the step-like initial distribution of plasma density shown in Figs.6 and 7.

5.6 Spectra of DW-ZF turbulence

Power spectra of residual fluctuations that, as we will show, persist for a long time after an initial density gradient has relaxed, are of significant practical importance. These fluctuations must profoundly impact radio wave transmission used for communication, geopositioning, and ionosphere probing purposes, to name a few (e.g., Kelly, 2012). Specific aspects of electromagnetic wave scattering from turbulent density layers have been discussed in (Sotnikov et al., 2008; V. I. Sotnikov et al., 2010; V. Sotnikov et al., 2014). As established earlier in this section, the fluctuations are confined to steep density gradients and strong shear flows. No significant turbulence spreading effects beyond its generation domain are observed for $\alpha \sim 1$. This turbulence confinement to the steep density gradient is still pertinent to a sufficiently broad range of the adiabaticity parameter α and other simulation parameters, such as the box size and aspect ratio. For significantly smaller values of α, however, initially sharp density contrasts broaden considerably after the instability progresses toward saturation. At the same time, limits are imposed on our simulation in this case. Nevertheless, sustainable boundaries with steep density gradients change the characteristics of the waves that pass through or are reflected by these boundaries. Moreover, a density trough with sharp edges will likely work as a duct for certain waves.

More specific effects of the relaxed density gradients on passing or reflected waves can be established by focusing on particular waves. Although this task is out of the scope of the present paper, a brief characterization of fluctuations and regular plasma motion inside the gradient areas is in order. The simulation results provide helpful information for wave interaction analyses with the relaxed plasma gradient. The most salient aspect of the regular motion is a strong shear with alternating flow directions. Given that it is formed in the area where the density drops may reach two orders of magnitude or even more, these flows should significantly impact the wave reflection from the dense plasma and mode conversion. The structure of the flow and its intensity can be gleaned from, e.g., Fig.9 and 10. These plots show rather typical flow and density profiles emerging after the relaxation of the initial density gradient with a moderate density contrast $\Delta n/n_0 \sim 10$. The number of strong ZF streams, three in this case, has increased in broader boxes for higher density contrasts and more strongly perturbed initial conditions. However, with varying simulation parameters, the flow preserves its morphology of alternating shear layers.

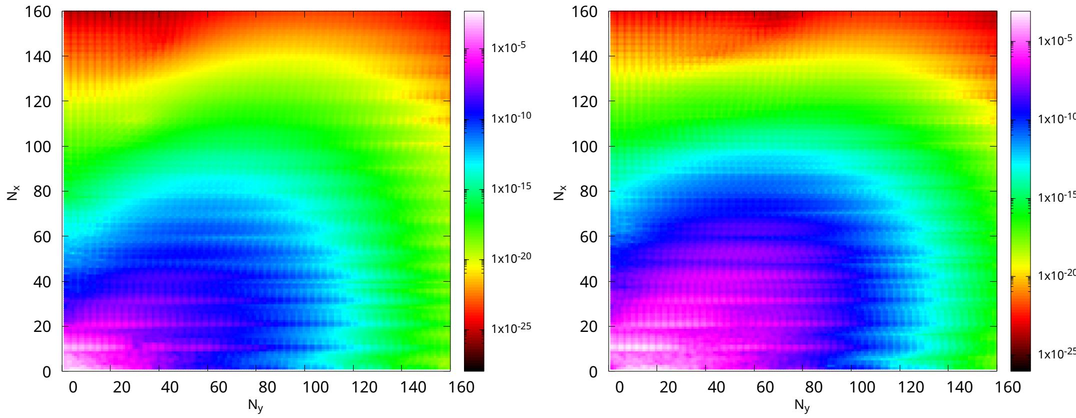

Figure 11. Density (left) and vorticity (right) power spectra, shown as functions of mode numbers in y and x directions.

These flows can be included in the overall power spectrum, manifesting several enhanced harmonics in k_y direction, or can be considered as a quasistationary background flow with superposed fluctuations. The choice of representation, again, depends on the wave scales that interact with the flow. For instance, the incoherent scatter radar technique that implies a radio frequency well above 100 MHz for some radar facilities with submeter wavelengths would probably rely on the second choice. If we project our results to a larger box (see, however, Sec.5.1), the scale of the shear flow may reach hundreds of meters or even more. However, depending on other control parameters, primarily the adiabaticity α and the density contrast Δn, the ZF profile may become much more oscillatory, which would *de facto* decrease the scale of the ZF.

To demonstrate a typical structure of the spectra emerging after the density gradient relaxation, we show in Fig.11 a 2D spectral density as a function of mode numbers in x and y direction. The spectrum is anisotropic at lower k and becomes more isotropic toward shorter scales of perturbations (higher N_x and N_y). One can also see visible modulations in the x direction likely produced by a nonlinear coupling of a few of the most unstable modes. For example, the flow is modulated at N_x=11 in the case shown in Fig.10. In addition, an isolated vortex is seen in this figure, both on the flow stream function and the density surface plot. The weak short-scale modulation in N_y, Fig.11, is due to the limited mode number and can be removed using finer grids, but without significant effects on the results.

More detailed information on the power spectra associated with the propagation of disturbances in the flow along the channel, i.e., DW propagation, can be obtained by integrating the spectrum over k_y. Such a spectrum is shown in Fig.12 for two times of integration. In both cases, the spectrum has an exponential form, which is best seen in a linear-log format. However, the spectrum shown at $t = 350$ (as other earlier spectra) has a distinct break at $k_x \approx 8$ with a clear steepening at higher k_x, especially pronounced in the flow vorticity. The exponential dependence of the spectrum below and above the break can be fitted as $\propto \exp\left(-k_x/k_c\right)$ with the "cut-off" $k_c = 1.23$ and 0.82, respectively.

At later times (e.g., $t = 700$, shown in Fig.12) the spectrum before the break steepens, showing a trend to asymptotically form a single exponent at high k_x with a cut-off $k_c = 0.82$. This happens earlier for the density fluctuations, as may be seen from the figure, but the overall spectra at higher k_x are very similar for density and vorticity perturbations. One may conclude that the coupling of the two equations (α- terms) are subdominant at short scales, and both n and $\Delta\Phi$ are convected with the same stream function Φ. This conclusion can be drawn directly from the equations.

At lower $k_x \gtrsim 1$, the intensity of the density perturbations drops precipitously, while the vorticity level decays at approximately the same rate as at higher k_x values below the break. Both vorticity and density fluctuations have a spectral maximum at $k_x \approx 1$, which stems from the maximum growth rate (outer scale of turbulence). Apart from the spectrum straightening at higher k_x, the scattering of modes around the respective exponential forms (straight lines in the linear-log format shown) diminishes.

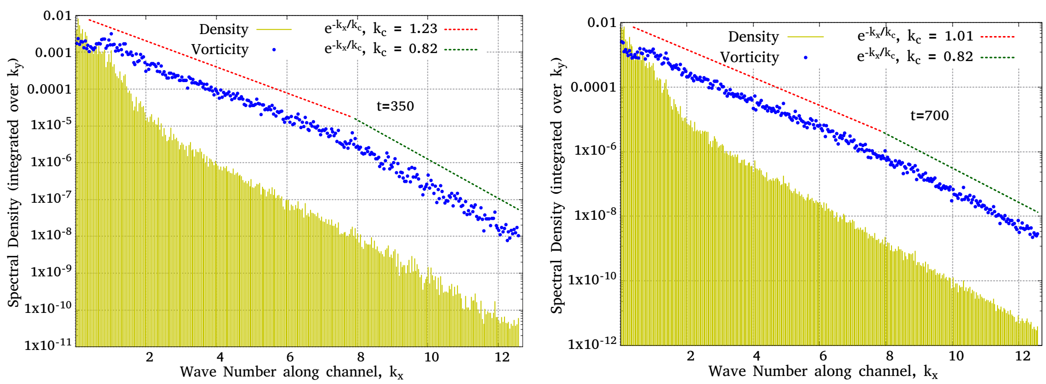

Figure 12. Power spectrum of density and vorticity perturbations integrated over k_y, The box size is $L_x \times L_y = 80 \times 40$, the respective number of grid points 1024x512.

6 Conclusions and Discussion

In this paper, we have investigated mesoscale dynamics in the Earth's ionosphere that we expect to accompany phenomena associated with *stormtime plasma density troughs*. Our focus was on the sharp plasma interfaces between high and low-density regions. These are thought to result from large-scale ionosphere instabilities, e.g., those of the Rayleigh-Taylor variety. They can also be formed by a rapid plasma evacuation along the magnetic field related to the ionosphere connection with the magnetosphere. Irrespective of their genesis, the density contrasts may undergo a secondary instability at much shorter scales, not accounted for by the primary mechanisms of their generation.

The development of a micro-scale instability in a certain parameter range, primarily where an adiabaticity parameter, $\alpha = k_z^2 V_{\mathrm{Te}}^2/\omega_{\mathrm{ci}}\nu_{\mathrm{ei}}$, does not strongly deviate from $\alpha \sim 1$, has profound consequences for mesoscopic and eventually macroscopic dynamics of the adjacent environment. We have investigated them in two basic settings. The first setting mimics a density trough, albeit limited in its transverse scale due to the code restrictions. To ease this limitation, we have studied in more detail the case of a density wall, which may represent either a part of a wide trough or an isolated density depletion in the ionosphere.

In both cases, we found that an unstable growth of plasma drift waves is accompanied by the generation of strong mesoscopic zonal flows (ZF) between the high and low-density regions, directed across the magnetic field. The shearing effect of the generated ZF on the transport-driving turbulence eddies lead to a substantial reduction of anomalous plasma diffusion. Consequently, we predict phenomena such as equatorial spread-

F plasma bubbles and density troughs (e.g., Huang et al., 2007), to be considerably more sustainable than mere drift-wave unstable density depletions. At the same time, a SAID phenomenon has been found (He et al., 2017) to have a large dispersion in its duration. One may assume that the underlying mechanisms behind the most protracted SAID events are sensitive to, and may even result from, specific ionospheric conditions at their locales. Whether these conditions correlate with the ZF generation requirements merits a separate observation analysis. The present study concludes that long-lifetime SAID are consistent with a strong flux suppression by the ZF generation. The required strong ZF streams are often seen near sharp density gradients in many observations (e.g., Huang et al., 2007).

We have also extracted detailed perturbation spectra from our simulation results. These data are necessary for probing the ionosphere by radar transmission using coherent and incoherent scatter and scintillation techniques (e.g., Kelly, 2012). In most cases with $\alpha \sim 1$, our code renders exponentially decaying fluctuation spectra. They can be straightforwardly fed into wave scattering models based on any observation techniques mentioned above. The choice of the density fluctuation spectrum is particularly crucial for the scintillation techniques.

Data Availability Statement

We have used the ISPACK software library for FFT transforms, documented in and publically available from, e.g., http://www.gfd-dennou.org/library/spmodel/label-2. The output from FORTRAN subroutines has been ported to Gnuplot, graphic software, also publically available at the Open Source Software repository at https://sourceforge.net/p/gnuplot/gnuplot-main/ci/master/tree/.

Acknowledgments

The authors are indebted to John Foster for his valuable comments. This work was supported by the Naval Research Laboratory Base Funds and the Air Force Office of Scientific Research. The paper is approved for Public Release. Info release number: IR-6754-24-1-U.

References

Balmforth, N. J., Smith, S. G. L., & Young, W. R. (1998, January). Dynamics of interfaces and layers in a stratified turbulent fluid. *Journal of Fluid Mechanics*, *355*, 329-358.

Basu, S., Basu, S., Valladares, C. E., Yeh, H.-C., Su, S.-Y., MacKenzie, E., ... Bullett, T. W. (2001). Ionospheric effects of major magnetic storms during the international space weather period of september and october 1999: Gps observations, vhf/uhf scintillations, and in situ density structures at middle and equatorial latitudes. *Journal of Geophysical Research: Space Physics*, *106*(A12), 30389-30413. Retrieved from `https://agupubs.onlinelibrary.wiley.com/doi/abs/10.1029/2001JA001116` doi: https://doi.org/10.1029/2001JA001116

Braginskii, S. I. (1965). Transport Processes in a Plasma. In (Vol. 1, p. 205).

Carreras, B. A., van Milligen, B., Pedrosa, M. A., Balbín, R., Hidalgo, C., Newman, D. E., ... Matthews, G. F. (1998, May). Long-range time correlations in plasma edge turbulence. *Phys. Rev. Lett.*, *80*, 4438–4441. Retrieved from `https://link.aps.org/doi/10.1103/PhysRevLett.80.4438` doi: 10.1103/PhysRevLett.80.4438

Dam, M., Brøns, M., Juul Rasmussen, J., Naulin, V., & Xu, G. (2013, October). Bifurcation analysis and dimension reduction of a predator-prey model for the L-H transition. *Physics of Plasmas*, *20*(10), 102302. doi: 10.1063/1.4823719

Diamond, P. H., Itoh, S.-I., Itoh, K., & Hahm, T. S. (2005, May). TOPICAL REVIEW: Zonal flows in plasma -a review. *Plasma Physics and Controlled Fusion*, *47*, 35-+. doi: 10.1088/0741-3335/47/5/R01

Dif-Pradalier, G., Hornung, G., Ghendrih, P., Sarazin, Y., Clairet, F., Vermare, L., … Storelli, A. (2015, February). Finding the Elusive ExB Staircase in Magnetized Plasmas. *Physical Review Letters*, *114*(8), 085004. doi: 10.1103/PhysRevLett.114.085004

Dippolito, D., Myra, J., & Zweben, S. (2011). Convective transport by intermittent blob-filaments: Comparison of theory and experiment. *Physics of Plasmas*, *18*(6).

Dritschel, D. G., & McIntyre, M. E. (2008). Multiple Jets as PV Staircases: The Phillips Effect and the Resilience of Eddy-Transport Barriers. *Journal of Atmospheric Sciences*, *65*, 855. doi: 10.1175/2007JAS2227.1

Estrada, T., Hidalgo, C., Happel, T., & Diamond, P. H. (2011, December). Spatiotemporal Structure of the Interaction between Turbulence and Flows at the L-H Transition in a Toroidal Plasma. *Phys. Rev. Lett.*, *107*(24), 245004. doi: 10.1103/PhysRevLett.107.245004

Foster, J. C., & Burke, W. J. (2002). Saps: A new categorization for sub-auroral electric fields. *Eos, Transactions American Geophysical Union*, *83*(36), 393-394. Retrieved from `https://agupubs.onlinelibrary.wiley.com/doi/abs/10.1029/2002EO000289` doi: 10.1029/2002EO000289

Garcia, O. E., Bian, N. H., Naulin, V., Nielsen, A. H., & Rasmussen, J. J. (2005, September). Mechanism and scaling for convection of isolated structures in nonuniformly magnetized plasmas. *Physics of Plasmas*, *12*(9), 090701-+. doi: 10.1063/1.2044487

Groebner, R. J., & Saarelma, S. (2023, may). Elements of h-mode pedestal structure. *Plasma Physics and Controlled Fusion*, *65*(7), 073001. Retrieved from `https://dx.doi.org/10.1088/1361-6587/acd478` doi: 10.1088/1361-6587/acd478

Guo, W., Diamond, P. H., Hughes, D. W., Wang, L., & Ashourvan, A. (2019, October). Scale selection and feedback loops for patterns in drift wave-zonal flow turbulence. *Plasma Physics and Controlled Fusion*, *61*(10), 105002. doi: 10.1088/1361-6587/ab3831

Hahm, T., & Diamond, P. (2018). Mesoscopic transport events and the breakdown of ficks law for turbulent fluxes. *Journal of the Korean Physical Society*, *73*, 747–792.

Hasegawa, A., & Wakatani, M. (1987, October). Self-organization of electrostatic turbulence in a cylindrical plasma. *Physical Review Letters*, *59*, 1581-1584. doi: 10.1103/PhysRevLett.59.1581

He, F., Zhang, X.-X., Wang, W., & Wan, W. (2017). Different evolution patterns of subauroral polarization streams (saps) during intense storms and quiet time substorms. *Geophysical Research Letters*, *44*(21), 10,796-10,804. Retrieved from `https://agupubs.onlinelibrary.wiley.com/doi/abs/10.1002/2017GL075449` doi: 10.1002/2017GL075449

Hinton, F. L., & Horton, C. W. (1971). Amplitude limitation of a collisional drift wave instability. *The Physics of Fluids*, *14*(1), 116-123. Retrieved from `https://aip.scitation.org/doi/abs/10.1063/1.1693260` doi: 10.1063/1.1693260

Horton, W. (1990, August). Nonlinear drift waves and transport in magnetized plasma. *Phys. Rep.*, *192*(1-3), 1-177. doi: 10.1016/0370-1573(90)90148-U

Huang, C.-S., Foster, J. C., & Sahai, Y. (2007). Significant depletions of the ionospheric plasma density at middle latitudes: A possible signature of equatorial spread f bubbles near the plasmapause. *Journal of Geophysical Research: Space Physics*, *112*(A5). Retrieved from `https://agupubs.onlinelibrary.wiley.com/doi/abs/10.1029/2007JA012307` doi: 10.1029/2007JA012307

Kelly, M. (2012). *The earth's ionosphere: Plasma physics and electrodynamics* (Vol. 43). Elsevier.

Kim, E.-J., & Diamond, P. H. (2003, May). Zonal Flows and Transient Dynamics of the L-H Transition. *Physical Review Letters*, *90*(18), 185006-+. doi: 10.1103/PhysRevLett.90.185006

Kim, Y. J., Imadera, K., Kishimoto, Y., & Hahm, T. S. (2022, October). Transport events and E × B staircase in flux-driven gyrokinetic simulation of ion temperature gradient turbulence. *Journal of Korean Physical Society*, *81*(7), 636-645. doi: 10.1007/s40042-022-00580-1

Ledvina, B. M., Makela, J. J., & Kintner, P. M. (2002). First observations of intense gps l1 amplitude scintillations at midlatitude. *Geophysical Research Letters*, *29*(14), 4-1-4-4. Retrieved from `https://agupubs.onlinelibrary.wiley.com/doi/abs/10.1029/2002GL014770` doi: https://doi.org/10.1029/2002GL014770

Liang, J., St-Maurice, J. P., & Donovan, E. (2021). A time-dependent two-dimensional model simulation of lower ionospheric variations under intense said. *Journal of Geophysical Research: Space Physics*, *126*(12), e2021JA029756. Retrieved from `https://agupubs.onlinelibrary.wiley.com/doi/abs/10.1029/2021JA029756` (e2021JA029756 2021JA029756) doi: https://doi.org/10.1029/2021JA029756

Liang, J., St-Maurice, J.-P., & Donovan, E. F. (2022). Model simulation of said intensification in the ionosphere under a current generator: The role of ion pedersen transport. *Journal of Geophysical Research: Space Physics*, *127*(11), e2022JA030960. Retrieved from `https://agupubs.onlinelibrary.wiley.com/doi/abs/10.1029/2022JA030960` (e2022JA030960 2022JA030960) doi: https://doi.org/10.1029/2022JA030960

MacDonald, E. A., Donovan, E., Nishimura, Y., Case, N. A., Gillies, D. M., Gallardo-Lacourt, B., ... others (2018). New science in plain sight: Citizen scientists lead to the discovery of optical structure in the upper atmosphere. *Science advances*, *4*(3), eaaq0030.

Malkov, M. A., & Diamond, P. H. (2009, #jan#). Weak hysteresis in a simplified model of the L-H transition. *Physics of Plasmas*, *16*(1), 012504-+. doi: 10.1063/1.3062834

Malkov, M. A., & Diamond, P. H. (2019, Apr). Dynamics of potential vorticity staircase evolution and step mergers in a reduced model of beta-plane turbulence. *Physical Review Fluids*, *4*, 044503. doi: 10.1103/PhysRevFluids.4.044503

Malkov, M. A., Diamond, P. H., & Rosenbluth, M. N. (2001, #dec#). On the nature of bursting in transport and turbulence in drift wave-zonal flow systems. *Physics of Plasmas*, *8*, 5073-5076.

Martinis, C., Griffin, I., Gallardo-Lacourt, B., Wroten, J., Nishimura, Y., Baumgardner, J., & Knudsen, D. J. (2022). Rainbow of the night: First direct observation of a sar arc evolving into steve. *Geophysical Research Letters*, *49*(11), e2022GL098511. Retrieved from `https://agupubs.onlinelibrary.wiley.com/doi/abs/10.1029/2022GL098511` (e2022GL098511 2022GL098511) doi: https://doi.org/10.1029/2022GL098511

Milovanov, A. V., Rasmussen, J. J., & Dif-Pradalier, G. (2021, May). Self-consistent model of the plasma staircase and nonlinear Schrödinger equation with subquadratic power nonlinearity. *Phys. Rev. E*, *103*(5), 052218. doi: 10.1103/PhysRevE.103.052218

Mishin, E., Nishimura, Y., & Foster, J. (2017). Saps/said revisited: A causal relation to the substorm current wedge. *Journal of Geophysical Research: Space Physics*, *122*(8), 8516-8535. Retrieved from `https://agupubs.onlinelibrary.wiley.com/doi/abs/10.1002/2017JA024263` doi: https://doi.org/10.1002/2017JA024263

Mishin, E. V. (2013). Interaction of substorm injections with the subauroral geospace: 1. multispacecraft observations of said. *Journal of Geophysical Research: Space Physics*, *118*(9), 5782-5796. Retrieved from `https://agupubs.onlinelibrary.wiley.com/doi/abs/10.1002/jgra.50548` doi: https://doi.org/10.1002/jgra.50548

Mishin, E. V. (2023). The evolving paradigm of the subauroral geospace. *Frontiers in Astronomy and Space Sciences*, *10*, 1118758.

Mishin, E. V., Burke, W. J., Huang, C. Y., & Rich, F. J. (2003, August). Electromagnetic wave structures within subauroral polarization streams. *Journal of Geophysical Research (Space Physics)*, *108*(A8), 1309. doi: 10.1029/2002JA009793

Mishin, E. V., & Streltsov, A. V. (2024). Toward the unified theory of said-linked subauroral arcs. *Journal of Geophysical Research: Space Physics*, *129*(1), e2023JA032196. Retrieved from `https://agupubs.onlinelibrary.wiley.com/doi/abs/10.1029/2023JA032196` (e2023JA032196 2023JA032196) doi: https://doi.org/10.1029/2023JA032196

Nishimura, Y., Dyer, A., Kangas, L., Donovan, E., & Angelopoulos, V. (2023). Unsolved problems in strong thermal emission velocity enhancement (steve) and the picket fence. *Frontiers in Astronomy and Space Sciences*, *10*, 1087974.

Nishimura, Y., Mrak, S., Semeter, J. L., Coster, A. J., Jayachandran, P. T., Groves, K. M., … Ruohoniemi, J. M. (2021). Evolution of mid-latitude density irregularities and scintillation in north america during the 7–8 september 2017 storm. *Journal of Geophysical Research: Space Physics*, *126*(6), e2021JA029192. Retrieved from `https://agupubs.onlinelibrary.wiley.com/doi/abs/10.1029/2021JA029192` (e2021JA029192 2021JA029192) doi: https://doi.org/10.1029/2021JA029192

Numata, R., Ball, R., & Dewar, R. L. (2007). Bifurcation in electrostatic resistive drift wave turbulence. *Physics of Plasmas*, *14*(10), 102312. Retrieved from `https://doi.org/10.1063/1.2796106` doi: 10.1063/1.2796106

Ossakow, S. L., & Chaturvedi, P. K. (1978). Morphological studies of rising equatorial spread f bubbles. *Journal of Geophysical Research: Space Physics*, *83*(A5), 2085-2090. Retrieved from `https://agupubs.onlinelibrary.wiley.com/doi/abs/10.1029/JA083iA05p02085` doi: https://doi.org/10.1029/JA083iA05p02085

Ott, E. (1978). Theory of rayleigh-taylor bubbles in the equatorial ionosphere. *Journal of Geophysical Research: Space Physics*, *83*(A5), 2066-2070. Retrieved from `https://agupubs.onlinelibrary.wiley.com/doi/abs/10.1029/JA083iA05p02066` doi: https://doi.org/10.1029/JA083iA05p02066

Pradipta, R., Mishin, E., & Groves, K. M. (2023). Storm-time subauroral ionospheric plasma density irregularities and the substorm current wedge. *Journal of Geophysical Research: Space Physics*, *128*(6), e2023JA031465. Retrieved from `https://agupubs.onlinelibrary.wiley.com/doi/abs/10.1029/2023JA031465` (e2023JA031465 2023JA031465) doi: https://doi.org/10.1029/2023JA031465

Pružina, P., Hughes, D. W., & Pegler, S. S. (2022, October). Development and long-term evolution of density staircases in stirred stratified turbulence. *Physical Review Fluids*, *7*(10), 104801. doi: 10.1103/PhysRevFluids.7.104801

Rogers, B. N., Dorland, W., & Kotschenreuther, M. (2000, December). Generation and Stability of Zonal Flows in Ion-Temperature-Gradient Mode Turbulence. *Physical Review Letters*, *85*, 5336-5339. doi: 10.1103/PhysRevLett.85.5336

Schmitz, L., Zeng, L., Rhodes, T. L., Hillesheim, J. C., Doyle, E. J., Groebner, R. J., … Wang, G. (2012, Apr). Role of zonal flow predator-prey oscillations in triggering the transition to h-mode confinement. *Phys. Rev. Lett.*, *108*, 155002. Retrieved from `http://link.aps.org/doi/10.1103/PhysRevLett.108.155002` doi: 10.1103/PhysRevLett.108.155002

Sinevich, A. A., Chernyshov, A. A., Chugunin, D. V., Oinats, A. V., Clausen, L. B. N., Miloch, W. J., … Mogilevsky, M. M. (2022). Small-scale irregularities within polarization jet/said during geomagnetic activity. *Geophysical Research Letters*, *49*(8), e2021GL097107. Retrieved from `https://agupubs.onlinelibrary.wiley.com/doi/abs/10.1029/2021GL097107` (e2021GL097107 2021GL097107) doi: https://doi.org/10.1029/2021GL097107

Sotnikov, V., Ivanov, V., Presura, R., Leboeuf, J., Onishchenko, O., Oliver, B., … Deeney, C. (2008). Investigation of compressible electromagnetic flute mode instability in finite beta plasma in support of z-pinch and laboratory astrophysics experiments. *Comput. Phys*, *4*, 611–623.

Sotnikov, V., Kim, T., Lundberg, J., Paraschiv, I., & Mehlhorn, T. A. (2014, May). Scattering of electromagnetic waves by vortex density structures associated with interchange instability: Analytical and large scale plasma simulation results. *Physics of Plasmas*, *21*(5), 052309. doi: 10.1063/1.4879021

Sotnikov, V. I., Leboeuf, J. N., & Mudaliar, S. (2010, September). Scattering of Electromagnetic Waves in the Presence of Wave Turbulence Excited by a Flow With Velocity Shear. *IEEE Transactions on Plasma Science*, *38*(9), 2208-2218. doi: 10.1109/TPS.2010.2049664

Tsunoda, R. T. (1988). High-latitude f region irregularities: A review and synthesis. *Reviews of Geophysics*, *26*(4), 719-760. Retrieved from `https://agupubs.onlinelibrary.wiley.com/doi/abs/10.1029/RG026i004p00719` doi: 10.1029/RG026i004p00719

Wagner, F., Becker, G., Behringer, K., Campbell, D., Eberhagen, A., Engelhardt, W., … Yü, Z. (1982, November). Regime of Improved Confinement and High Beta in Neutral-Beam-Heated Divertor Discharges of the ASDEX Tokamak. *Physical Review Letters*, *49*, 1408-1412. doi: 10.1103/PhysRevLett.49.1408

Zweben, S., Maqueda, R., Stotler, D., Keesee, A., Boedo, J., Bush, C., … others (2003). High-speed imaging of edge turbulence in nstx. *Nuclear Fusion*, *44*(1), 134.